American Mineralogist, Volume 88, pages 763–769, 2003

X-ray absorption spectroscopy of silicates for in situ, sub-micrometer mineral identification

B. GILBERT,[1] B.H. FRAZER,[1,2] F. NAAB,[3] J. FOURNELLE,[4] J.W. VALLEY,[4] AND G. DE STASIO[1,*]

[1]University of Wisconsin, Department of Physics, and Synchrotron Radiation Center, 3731 Schneider Drive, Stoughton, Wisconsin, 53589, U.S.A.
[2]Institut de Physique Appliquee, Ecole Polytechnique Federale de Lausanne, CH-1015 Lausanne, Switzerland
[3]University of Notre Dame, Department of Physics, Notre Dame, Indiana 46556, U.S.A.
[4]University of Wisconsin, Department of Geology and Geophysics, Madison, Wisconsin, 53706, U.S.A.

ABSTRACT

We present X-ray absorption near-edge structure (XANES) spectroscopy of 11 silicate and aluminosilicate minerals and two glasses at the Si*K* and Si$L_{2,3}$, and O*K* edges. The similar nearest-neighbor environments lead to similar spectral lineshapes at each edge, but the fine-structure differences allow individual and groups of structurally similar minerals to be distinguished. By combining spectra and their first energy derivative from three absorption edges, we show that every mineral studied is distinguishable with XANES. This background work, combined with X-ray PhotoElectron Emission spectroMicroscopy (X-PEEM), allows non-destructive in situ, sub-micrometer (to 35 nm) X-ray analysis of materials, including silicate inclusions, which has not been possible previously. Images and spectra from a 7 μm × 3.5 μm quartz inclusion in zircon are presented as a test of this novel technique in geology.

INTRODUCTION

The rock-forming silicate minerals exhibit a rich diversity of crystal structure, obtained through patterns of Si-O linking (pure SiO_2 alone exhibits eight polymorphs and many more glassy phases) and cation incorporation, such as Al, Fe, and the alkali metals. Electron diffraction, X-ray diffraction, and electron microprobe analysis are firmly established as robust methods of silicate mineral identification, but the latter two techniques do not allow sub-micrometer resolution. Selected-area electron diffraction has higher resolution, but it requires destructive ion milling. X-ray absorption near-edge structure (XANES) is element-specific and is used both as a probe of bonding and as a fingerprint for certain local coordination geometries (Wilke et al. 2001). Here we explore the potential for X-ray absorption spectroscopy to provide an absolute method of silicate mineral identification. XANES can be coupled with high resolution X-ray photoelectron emission spectroMicroscopy (X-PEEM) (Bauer 2001), for spatially resolved chemical analysis of mineral inclusions on the micrometer and submicrometer scale, with optimum resolution of 6 nm (De Stasio et al. 2001). XANES spectroscopy is equivalent to electron energy-loss spectroscopy (EELS) (Garvie and Buseck 1999), but allows analysis of thick samples, is surface sensitive, and non-destructive to polished grain mounts or thin sections.

The sensitivity of XANES to crystal structure is strongly dependent on the nature of the final states of the X-ray absorption process, which may vary at different absorption edges of an element. For example, transition metal *L* edge absorption is frequently sensitive to atomic charge and nearest-neighbor coordination (Grush et al. 1996; Wang et al. 1997). The sensitivity of X-ray absorption to structural modifications beyond the nearest-neighbor environment has not been fully explored. We have previously shown that $L_{2,3}$ edge X-ray absorption is sensitive to *cubic-hexagonal* polymorphism in II-VI semiconductors, for which the nearest-neighbor positions are unchanged, and that this modification is not detectable with *K*-edge absorption (Gilbert et al. 2002). Si occurs within SiO_4 tetrahedra in all the minerals analyzed in this study.

Evidence already exists that XANES spectroscopy of silicates may allow species identification. Using large cluster molecular orbital calculations, other authors have concluded that the unoccupied states are more sensitive than the valence band to the details of SiO_4 tetrahedral linkage in silicates (Tanaka et al. 1995). A recent large study of Si$L_{2,3}$ EELS showed excellent discrimination between and within nesosilicate, inosilicate, and sorosilicate classes (Garvie and Buseck 1999). By contrast, lineshapes within the tectosilicate and phyllosilicate classes were far less distinct. The present study addresses this problem. We use X-ray absorption spectra at the Si*K* and Si$L_{2,3}$ edges, and the O*K* edge of selected silicates to observe the relative sensitivity of each absorption edge to different silicate structures. The minerals in this study were selected to distinguish feldspar, quartz, or silicate glass inclusions in zircons (Peck et al. 2001).

EXPERIMENTAL METHODS

Portions of the silicate samples listed in Table 1 have been chemically analyzed and imaged by electron microprobe analysis (Table 2). In separate preparations, pieces were powdered and pressed into soft indium metal. X-ray absorption spectra were acquired in the total electron yield (TEY) mode at the University of Wisconsin Synchrotron Radiation Center, on the HERMON beamline (Si$L_{2,3}$ edge, O*K* edge, Ca$L_{2,3}$ edge; < 0.1 eV resolution), the 6m TGM beamline (Si$L_{2,3}$ edge; 0.1 eV resolution), and the DCM beamline (Si*K* edge; < 0.5 eV resolution). Si$L_{2,3}$ edge spectra acquired on both 6 m TGM and HERMON beamlines are presented. Si$L_{2,3}$ XANES from quartz taken on the two beamlines were compared to ensure that there are no detectable differences in energy resolution and absolute

* E-mail: pupa@src.wisc.edu

TABLE 1. The silicate minerals for this study

Compound	Ideal formula	ID no.	abbrev.
	tectosilicates		
α-quartz no. 1	SiO_2	——	Qua
α-quartz no. 3	SiO_2	8015 Nova Scotia	Qua
α-quartz no. 2	SiO_2	5016 Minas Gerais	Qua
Microcline no. 1	$KAlSi_3O_8$	7062	Mic
Microcline no. 2	$KAlSi_3O_8$	7085	Mic
Albite	$NaAlSi_3O_8$	7104	Alb
Sanidine	$K_{0.75}Na_{0.25}AlSi_3O_8$	IP96-1	San
Andesine	$Na_{0.6}Ca_{0.4}Al_{1.4}Si_{2.6}O_8$	7144	And
Adularia	$KAlSi_3O_8$	St. Gotthard	Adu
Bytownite	$Ca_{0.8}Na_{0.2}Al_{1.8}Si_{2.2}O_8$	Crystal Bay	Byt
	phyllosilicates		
Muscovite	$KAl_2AlSi_3O_{10}(OH)_2$	8109 A	Mus
Biotite	$K(MgFe)_3AlSi_3O_{10}(OH)_2$	8131	Bio
Apophyllite	$(K,Na)Ca_4Si_8O_{20}(F,OH)(H_2O)_8$	8012 A	Apo
	nesosilicates		
Zircon no. 1	$ZrSiO_4$	R18113	Zir
Zircon no. 2	$ZrSiO_4$	7288-2	Zir
	glasses		
Obsidian		QER16	Obs
Rhyolite		IP96-1	Rhy

TABLE 2. Electron microprobe analysis of minerals and glass

	Andesine[1]		Albite[2]		Microcline[3]		Microcline[4]		Adularia[5]
	7144		7104		7085		7062		
no. pts.	18	sd	20	sd	19	sd	20	sd	1
SiO_2	58.74	0.71	68.29	0.97	64.76	0.63	64.26	0.94	64.28
TiO_2									
Al_2O_3	26.33	0.38	19.85	0.22	18.42	0.30	18.85	0.19	19.20
Fe_2O_3									0.09
FeO	0.03	0.03	<.02		<.02		0.03	0.04	
MnO									
MgO									0.10
CaO	7.76	0.25	0.14	0.11	<.01		<.01		0.11
Na_2O	7.04	0.17	11.01	0.21	0.50	0.10	0.64	0.16	0.92
K_2O	0.09	0.1	0.14	0.07	16.08	0.17	15.99	0.34	15.3
F									
H_2O									
Total	99.99		99.45		99.78		99.79		99.99
"-F=O"									
Total									
Norm.*	8		8		8		8		8
Si	2.621		2.992		2.997		2.976		2.963
Ti									
Al	1.385		1.025		1.005		1.029		1.042
Fe^{+3}									
Fe^{+2}	0.001						0.001		0.003
Mn									
MgO									0.007
Ca	0.371		0.007		0		0		0.005
Na	0.609		0.936		0.045		0.057		0.082
K	0.005		0.008		0.949		0.945		0.899
F									
OH									
Sum	12.99		12.97		12.997		13.01		5
Ab	61.8		98.5		4.5		5.7		8.3
An	37.7		0.7		0		0.1		0.5
Or	0.5		0.8		95.5		94.2		91.2

energy calibration. The two beamlines do vary in higher-order X-ray rejection, and hence Ca third-order contributions are present in S$L_{2,3}$ edge spectra from Ca-containing silicates studied on the HERMON beamline only. The energy step in Si$L_{2,3}$ and OK spectra is 0.2 eV. Each spectrum is composed of at least 3 separate scans from a single specimen and preparation.

TABLE 2—continued

	Apophyllite[8]		Biotite[9,10]		Muscovite[9,11]		Bytownite[14]	
	8012A		8131		8109A		An78	
no. pts.	20	sd	17	sd	16	sd	75	sd
SiO_2	52.60	0.47	34.16	0.80	44.63	0.39	47.52	0.74
TiO_2	<.01		2.22	0.11	0.16	0.05		
Al_2O_3	0.27	0.08	18.95	0.50	33.22	0.50	32.90	0.33
Fe_2O_3			10.60		3.99	0.27		
FeO	<.03		14.30	0.54	0.00		0.37	0.08
MnO	<.03		0.18	0.09	0.07	0.05		
MgO	<.01		6.03	0.12	1.08	0.07	0.12	0.03
CaO	24.27	0.26	0.04	0.03	<.02		15.75	0.27
Na_2O	0.16	0.04	0.22	0.05	0.44	0.10	2.53	0.12
K_2O	4.75	0.2	9.04	0.3	10.51	0.26	0.07	0.03
F	2.44	0.4	0.17	0.1	0.69			
H_2O	15.70		3.80		4.05			
Total								
"-F=O"	–1.03		–0.07		–0.29			
Total	99.21		99.63		98.56		99.27	0.90
Norm.*	28		24(O+F)		24(O+F)			
8								
Si	8.029		5.214		6.08		2.196	
Ti	0.002		0.255		0.016			
Al	0.049		3.409		5.335		1.792	
Fe^{+3}			0.761		0.409			
Fe^{+2}	0.002		2.282				0.011	
Mn	0.002		0.023		0.007			
MgO	0.001		1.371		0.22		0.009	
Ca	3.969		0.007		0.001		0.780	0.015
Na	0.047		0.066		0.116		0.227	
K	0.925		1.759		1.827		0.004	
F	1.18		0.083		0.299			

Two different samples from different geologic environments were obtained for zircon and microcline, and three for quartz, to ensure the consistency of the spectra, independent of mineral origin.

Experimental XANES spectra must be normalized to remove the background energy dependence of the X-ray monochromator, which is strongly curved at the Si$L_{2,3}$ edge. The electron yield current was simultaneously recorded from a nickel mesh during each measurement, but this did not give a satisfactory normalization for the Si$L_{2,3}$ edge spectra. Instead, the most consistent results were obtained by dividing the experimental data by a polynomial fitted to the data before 100 eV and after 130 eV. This approach is commonly applied to XANES in the soft X-ray energy region (Wang et al. 1997; Li et al. 1994).

The Spectromicroscope for photoelectron imaging of nanostructures with X-rays (SPHINX, Elmitec GmbH), our X-ray photoelectron microscope (X-PEEM) (Bauer 2001; De Stasio et al. 1998), collects and images secondary electrons emitted from a specimen surface under X-ray illumination, using high voltage (–20 kV) extraction and magnetic electron lenses. The secondary electron intensity is proportional to the local X-ray absorption cross section, providing simultaneous specimen imaging and XANES analysis from microscopic areas. Strongly insulating samples, such as silicate mineral surfaces, have been impossible to study with this technique due to severe charging effects. However, we have recently optimized a method of coating surfaces with a metallic film, described below, which is sufficiently continuous to overcome charging, yet thin enough that the short range, XANES signal-carrying, secondary electrons are emitted from the specimen beneath.

Zircons from Jack Hills (Australia) (Peck et al. 2001), not previously analyzed or dated, were embedded in epoxy resin,

TABLE 2—continued

	Zircon[12]		Zircon[13]			Obsidian[6]		Rhyolite[7]
	7288-2		R18113			QER16		IP96-1
no. pts.	20	sd		sd		30	sd	1
ZrO_2	66.90	0.90	66.88	0.79	SiO2	75.34	0.51	76.90
HfO_2	1.25	0.09	0.96	0.37	TiO2	0.12	0.04	0.13
SiO_2	32.66	0.80	32.81	0.70	Al2O3	13.40	0.18	12.30
Y_2O_3	<.01		<.01		Fe2O3			2.00
ThO_2	<.01		<.01		FeO	0.93	0.13	
UO_2	<.01		<.01		MnO	0.05	0.04	0.08
Yb_2O_3	<.01		<.01		MgO	0.07	0.03	<0.01
					CaO	0.67	0.06	0.45
Total	100.82		100.66		Na2O	2.93	0.18	3.44
					K2O	5.19	0.16	4.51
					F	0.07	0.11	
Norm.*	4		4		H2O			0.25 (LOI)
Zr	0.994		0.993		Total			
Hf	0.011		0.008		"-F=O"	-0.03		
Si	0.995		0.999		Total	98.74		
Sum	2.000		2.000					

Notes: no. pts. = number of points analyzed; sd=absolute std dev between points; mdl=99% level detection limit. 1 = Sannida, Norway; has some zonation; 5 = other analyses (excluded) range from An_{10}-An_{44}. 2 = Amelia Court House, Virginia. 3 = Amelia Court House, Virginia; has some albite lamellae (excluded). 4 = Micanite, Freemont County, California; has some albite lamellae (excluded). 5 = St. Gotthard, Switz. 6 = Early rhyolite, Long Valley, Calif. 7 = Bishop Mountain flow. Island Park caldera, Idaho. 8 = H_2O calculation based upon 8 H_2O per Si_8O_{20} formula; oxygen included within matrix correction. 9 = H_2O based upon $O_{20}(OH,F)_4$ formula and Fe^{+3}/Fe^{+2} by charge balance. Oxygen included in matrix correction. Fe std dev is for Fe-total. 10 = Murray Bay, Quebec. 11 = Canon City, Colorado. 12 = USNM no. 117288-2, Strangeway, N. Territory, Australia. 13 = USNM no. R18113, Mogok, Burma. 14 = An78. Crystal Bay. Homogeneous plagioclase, analysis of 9 chips. Operating conditions: 15 kV, 10 nA, 5 mm defocused beam for silicates. Obsidian, 6 nA. Counting time 10 seconds peak and equal on backgrounds. Zircons: 18 kV, 20 nA for Zr, Hf, Si. Trace elements at 200 nA for 20 sec equal peak and bkg count times.
*Norm.: normalized to 4, 8, 24, or 28 oxygen atoms.

and polished with 0.1 μm diamond powder. Following double cleaning in an ultrasonic bath with ethanol and distilled water, we sputter-coated 1 nm Pt/Pd (80%/20%) onto the surface at 1.5×10^{-2} Torr (Cressington, U.K.). The sample was then transferred to SPHINX, installed on a 6m TGM beamline, imaged, and analyzed at the Si$L_{2,3}$ edge at a base pressure of 10^{-10} Torr.

RESULTS AND ANALYSIS

The experimental XANES of the silicates are presented in Figures 1–3. Where spectra of the silicates chosen in this study have been published previously, there is excellent agreement [α-quartz Si$L_{2,3}$ edge (Garvie and Buseck 1999; Li et al. 1994), Si*K* edge (Li et al. 1995), and O*K* edge (Wu et al. 1998); albite Si*K* edge (Calas et al. 1987), and Si$L_{2,3}$ edge (Garvie and Buseck 1999); muscovite Si$L_{2,3}$ edge (Garvie and Buseck 1999); zircon Si$L_{2,3}$ edge, Si*K* edge, and O*K* edge (McComb et al.1992); microcline Si*K* edge (Li et al. 1995)]. Silicates from different geological environments (quartz, zircon, and microcline) produced very close spectra, although the low-energy pre-edge feature at the microcline O*K* edge (around 530 eV), varied in intensity between the two samples. The X-ray absorption spectra do not show finer energy resolution than corresponding EELS. As observed previously, with the exception of zircon, spectroscopy at each absorption edge produces a basic lineshape that is similar for all the silicates analyzed.

The spectra in Figures 1–3 have been normalized with no further treatment, and are hereafter called untreated spectra. In order to detect fine-structure differences in the experimental spectra, Figure 4 compares the 1st derivative of the Si$L_{2,3}$ edge and O*K* edge spectra (dI/dE) for the tectosilicate minerals studied, hereafter called derivative spectra. Figure 5 compares the equivalently treated spectra for the remaining silicates. Derivative spectra are a common way of visualizing very weak spectroscopic signals, as in secondary electron spectroscopy (Hoffman et al. 1991), and enhance the fine-structure in X-ray absorption investigations (Westre et al. 1997; Kisiel et al. 1989).

We analyzed the data set of Figures 1–5 and determined the sensitivity of XANES spectroscopy to the silicates studied. We assumed one of the following two criteria as sufficient for two spectra to be considered distinguishable. (1) There must be a peak[1] of 5 data points or more that does not appear in one spectrum, or is shifted by >1.0 eV. (2) The two spectra contain a peak at the same energy position that differ in normalized intensity, or in width, by >50%.

These experimental criteria are framed to test whether silicate minerals can be distinguished confidently by their XANES spectra. They take into account the limits of the technique, including experimental broadening, signal-to-noise ratio within acceptable counting times, and the reproducibility of monochromator calibration. Based on these criteria, we discriminate the experimental XANES spectra. The criteria are conservative, as both experiment and theory can distinguish fine-structure at higher resolution (Grush et al. 1996; Gilbert et al. 2002), but such features are not seen in silicate spectra. XANES linewidth is intrinsically limited by the lifetime of the core hole following X-ray absorption, but here the width of the unoccupied electronic band structure exceeds intrinsic and experimental broadening at the Si$L_{2,3}$ and O*K* edges. At the Si*K* edge, intrinsic broadening dominates.

For one of the minerals analyzed to be considered identifiable by XANES spectroscopy at one of the edges (untreated, or as the energy derivative), it must be distinguishable, according to the above criteria, from all other acquired spectra. The results of this analysis are given schematically in Figure 6.

There are only three silicates, bytownite, quartz and zircon, among the minerals studied that could be identified confidently based on the untreated spectrum at a single edge. Despite the similarity of the bytownite Si$L_{2,3}$ spectrum to those of other feldspars, the pre-peak in fact contains two contributions, not clearly visible in Figure 2, that can be resolved according to the above criteria. Unlike quartz and zircon, it is probable that bytownite would not remain distinguishable in a larger study of the feldspars.

If untreated data for all three absorption edges are available, the ability of the technique to distinguish the minerals studied is significantly improved. For example, albite is distinguishable from microcline only at the Si*K* edge, but at this edge, microcline and andesine are indistinguishable, and O*K* edge

[1] Inverse peaks are admitted in the case of energy derivative spectra.

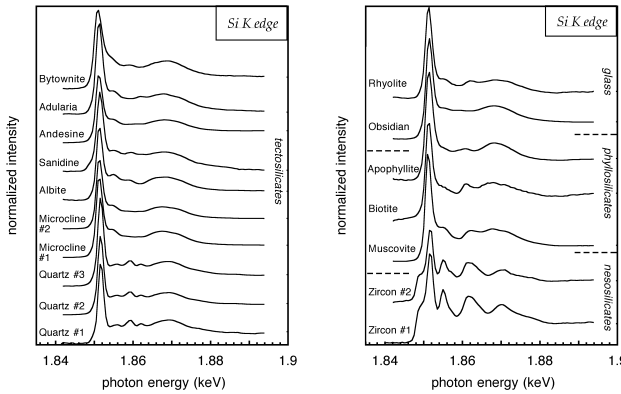

FIGURE 1. Si*K* edge XANES of tectosilicates (left) and nesosilicates, phyllosilicates, and glasses (right).

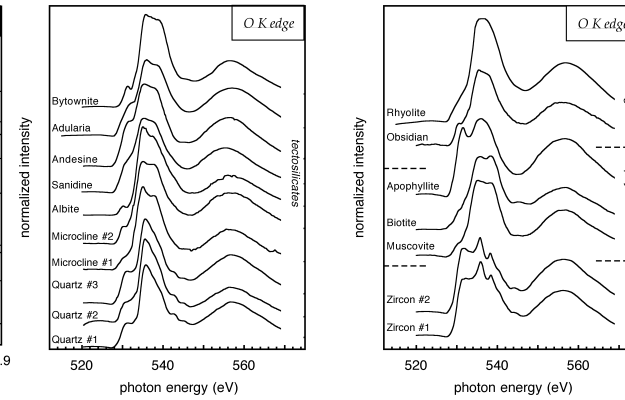

FIGURE 3. O*K* edge XANES of tectosilicates (left) and nesosilicates, phyllosilicates, and glasses (right).

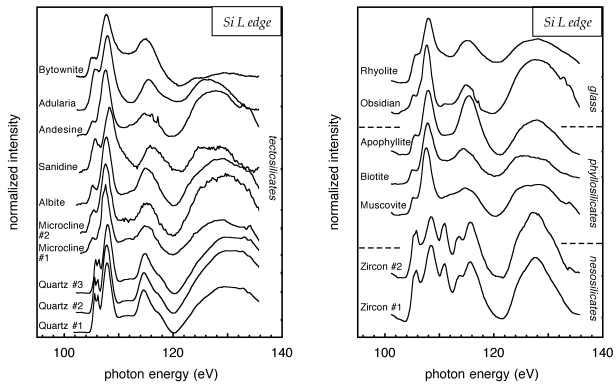

FIGURE 2. Si$L_{2,3}$ edge XANES of tectosilicates (left) and nesosilicates, phyllosilicates, and glasses (right). The small double peak around 118 eV on the andesine spectrum is due to Ca, whose L edge spectrum at 345 eV also appears at lower energy due to third-order transmission of the X-ray monochromator.

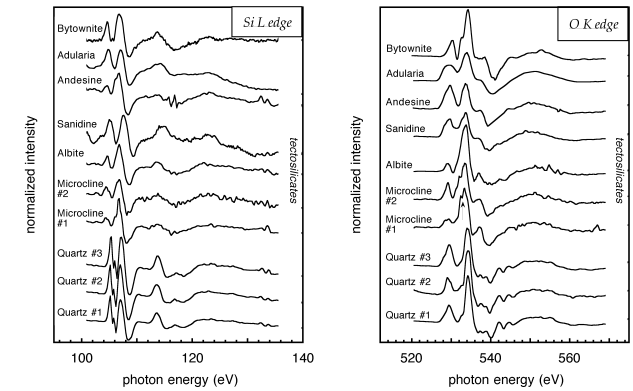

FIGURE 4. Energy derivatives of the Si$L_{2,3}$ (left) and O*K* (right) edge spectra from tectosilicates. The small double peak around 118 eV on the andesine spectrum is due to Ca*L* edge third order. The fine structure on the microcline O*K* edge derivative spectra (arrow) is reproducible, and distinguishes the lineshape from albite.

data are required to discriminate them. Obtaining the energy derivative of the Si$L_{2,3}$ and O*K* edge spectra increases the separation further. Note that treating the Si*K* edge spectra in this manner did not reveal structure, because the intrinsic broadening of X-ray absorption spectra increases with the energy of the absorption edge. In the O*K* edge derivative spectra, biotite and muscovite are distinguishable, and a fine difference appears between albite and both microcline samples.

Figure 6 indicates that the Si*K* edge offers the finest discrimination among the silicates studied, when untreated spectra are analyzed, but the O*K* edge is most reliable when fine-structure is enhanced by taking the energy derivative. If the Si$L_{2,3}$ and O*K* edge derivative spectra are both acquired, all of the minerals in this study can in principle be distinguished.

DISCUSSION

Structural information in electron and X-ray diffraction relies on plane wave scattering. By contrast, the structural probe of X-ray absorption is the spherical wave photoelectron that is multiply scattered from atomic sites in the vicinity of the absorber (Rehr and Albers 2000). Due to the relatively low energy of the photoelectron, the fine-structure is intimately connected to the unoccupied electronic states in the solid.

Many experimental and theoretical studies have addressed the electronic structure of the silicate minerals. The recurring structural unit is the SiO_4 tetrahedron, and many authors have focussed on this unit in theoretical (Tossell 1975) and experimental (Sutherland et al. 1993) investigations. Nearest-neighbor atoms have the greatest influence on the electronic structure of a photoexcited atom, and hence on X-ray absorption fine-structure. This conclusion is clear from the strong similarities in the underlying absorption lineshapes in Figures 1–3 (with the exception of zircon, discussed below), and from the success of nearest-neighbor molecular orbital (MO) calculations (Tossell 1975).

In real silicates, however, the SiO_4 tetrahedron is distorted, and/or cross linked through up to four bridging oxygen atoms to neighboring tetrahedra. Some correlations are observed between the geometry of the SiO_4 unit and the physical properties of silicates (de Jong and Brown 1980; Li and Ching 1985), such as a close linear correlation obtained between bond length and height of the insulating gap in the silica polymorphs. However, correlations between SiO_4 geometry and XANES are

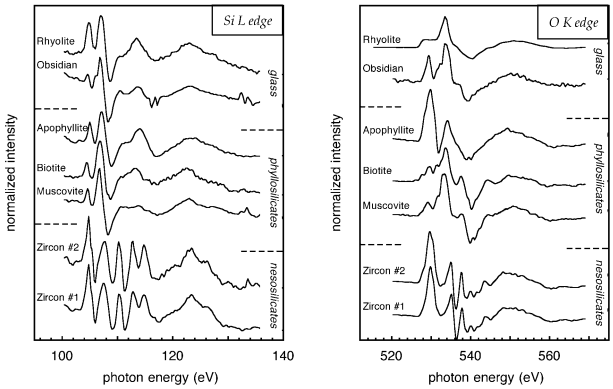

FIGURE 5. Energy derivatives of the Si$L_{2,3}$ (left) and O*K* (right) edge spectra from nesosilicates, phyllosilicates and glasses. The fine structure on the biotite O*K* edge derivative spectrum (arrow) is reproducible, and distinguishes the lineshape from muscovite.

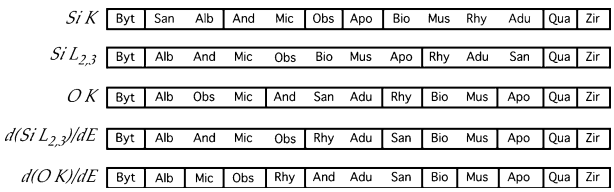

FIGURE 6. Scheme showing the sensitivity of XANES spectroscopy to the tectosilicates, phyllosilicates and glasses analyzed, at the important absorption edges (Figs. 1–3), and with energy-derivative spectra (Figs. 4 and 5). Silicates with indistinguishable spectra at a given X- ray absorption edge are displayed together within a box. The abbreviations refer to Table 1, and the criteria for distinguishable spectra are given in the text.

weaker (Garvie and Buseck 1999). The Si*K* absorption edge onset shows a trend toward higher energy with increase in the polymerization of the SiO_4 tetrahedra (Li et al. 1995).

Recent work suggests that for the understanding of XANES spectroscopy, a complete, long-range model of the material is required. An expansive survey of XANES spectra of silicates (Garvie and Buseck 1999) showed the significance of non-nearest-neighbor cations. MO calculations show significant energy level splitting for larger clusters [$H_6Si_2O_7$ (de Jong and Brown 1980; Geisinger et al. 1985), and Si_5O_{16} (Tanaka et al. 1995)] that offer better agreement with data. Furthermore, recent multiple scattering calculations have been shown to require large (100 atom) clusters to describe fully the experimental XANES of quartz (Wu et al. 1998) and stishovite (Soldatov et al. 2000).

The electronic structure of pure silica minerals

Molecular orbital studies (Tossell 1975; de Jong and Brown 1980; Geisinger et al. 1985) and band structure calculations (Li and Ching 1985; Garvie et al. 2000) of pure SiO_2 crystals give broadly the same picture of approximately sp^3 hybridization of the Si 3*s*, 3*p* levels and *sp* hybridization of the bridging oxygen 2*s*, 2*p* levels. Most valence electron density is in the vicinity of the O atom, consistent with a partly ionic crystal, with the upper valence band consisting of non-bonding O 2*p* states. The involvement of silicon 3*d* states, permitted for the Si site symmetry, has provoked some debate. Silicon 3*d* contributions to the valence states are probably negligible, but do play a significant role in the X-ray absorption spectrum from about 4 eV above threshold. Silicon s and p states dominate at threshold, with 3*s* states at the conduction band minimum.

Calculations have rather outpaced direct experimental investigations of electronic structure modification in the silica polymorphs. X-ray emission spectroscopy shows very small valence band differences among the 4-coordinated crystalline silica phases (Wiech and Kurmaev 1985). Broad spectra are a result of both the attainable resolution of the technique, as well as the formation of wide bands in crystals. By contrast, Si$L_{2,3}$ edge XANES studies of the polymorphs distinguished all the phases studied (Li et al. 1994).

The effect of non-network-forming cations and Al substitution

Interstitial cations can lead to large distortions of the SiO_4 tetrahedra and, more significantly, introduce extra electronic states. The importance of the non-network-forming (NNF) cations was first pointed out by Garvie and Buseck (1999), who realized that Si$L_{2,3}$ fine-structure in nesosilicates is more affected by the NNF cations than degree of SiO_4 distortion, contrary to previous reports. Multiple scattering calculations indicated that the striking difference between the spectra of zircon and the other silicates is entirely due to O hybridization

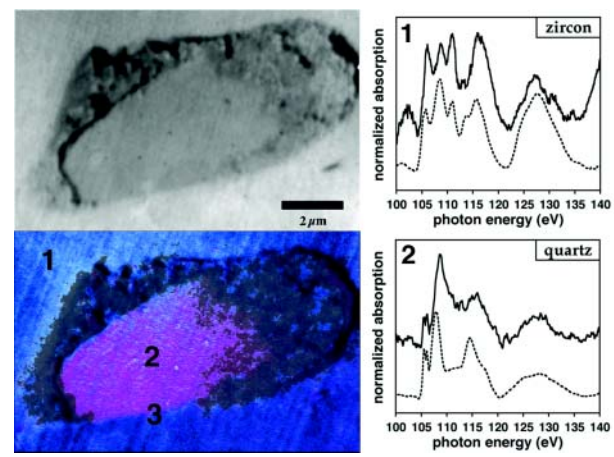

FIGURE 7. Chemical mapping of silicate species. The X-PEEM photoelectron micrograph in the top left image shows an unknown inclusion in zircon. XANES spectra acquired from regions 1 and 2 are given on the right, and allow identification of the inclusion as quartz. Solid curve = X-PEEM data; dashed curve = XANES of reference standard. Note that the quartz X-PEEM spectrum was taken from a single image pixel (35 nm ¥ 35 nm) in position 2. The separate quartz and zircon domains are mapped in the bottom left image: blue = zircon; pink = quartz; brown = no Si detected. The region from which no Si signal was detected is a pit, as observed in SEM. Carbon contamination in this pit prevents mineral analysis by surface-sensitive X-PEEM. There is a sharp quartz-zircon boundary in the vicinity of position 3. Two immediately adjacent pixels at this boundary give pure quartz and pure zircon spectra.

with Zr *4d* states situated at the conduction band minimum (McComb et al. 1992). *3d* states from Ca and transition metal cations are likely to affect XANES fine-structure in a similar way. From small cluster calculations, the effect of Al substitution is to further underbond the bridging O atom, leading to lone pair formation, contraction of the Si-O-Al bond angle, and enhanced possibility of hybridization with NNF cations required for charge stabilization (Geisinger et al. 1985). Al substitution is therefore likely to increase NNF cation effects on XANES spectra, but we are not aware of any calculations that have investigated this.

XANES of the alkali feldspars

The discrimination of feldspars from alternative silicates, and the identification of individual feldspar minerals is of particular interest. Although Figure 6 shows that the untreated spectra do not distinguish all the minerals in this study, the lineshapes at the O*K* edge sort the minerals into groups with similar crystal structures. Examples include albite and microcline as well as muscovite and biotite. This result offers the reassurance that even if future studies are not able to achieve full differentiation, unknown silicates are likely to be grouped correctly within a small subset of similar minerals. For example, using O*K* edge derivative spectra, it is possible to differentiate very well between the K- and Na-feldspars (in particular microcline vs. albite).

The similarity of the XANES lineshapes for glassy obsidian and crystalline microcline at the Si$L_{2,3}$ and O*K* edges is unexpected. Whereas at the Si$L_{2,3}$ and O*K* edges rhyolite exhibits the broad lineshape and early edge onset expected of amorphous samples, a single feature distinguishes obsidian and microcline in the O*K* derivative spectra. By contrast, the obsidian spectrum is distinct from all others at the Si*K* edge. The smooth lineshape at this edge is well modeled theoretically by a single SiO_4 tetrahedron (Wu et al. 1998), which may be expected of a material that is disordered beyond the first shell. As the medium range structure of amorphous materials is not well understood, the significance of the results at the Si$L_{2,3}$ and O*K* edges is not clear.

Within the feldspars, the Si$L_{2,3}$ and O*K* lineshapes are broader for minerals with a wide range of compositions, but our data are not able to address the causes of the broadening. A previous study reveals that the main peak of the Si$L_{2,3}$ edge of anorthite is significantly broader than for albite (Garvie and Buseck 1999). Similarly, in this work, the main Si$L_{2,3}$ peak of bytownite (shown in Table 2 to contain approximately 78% of the anorthite end-member) is much broader than the albite spectrum (Fig. 2). This lineshape broadening may be a consequence of Ca incorporation. However, we show in Figures 2 and 3 that andesine, adularia, and sanidine also have broader O*K* and Si$L_{2,3}$ lineshapes than albite or quartz, and so it is not possible to say whether this broadening is a result of the introduction of electronic states associated with cation substitution, or of tetrahedral distortion. We cannot address in this study the consequences of Al-Si disorder in feldspars (e.g., microcline vs. sanidine) on XANES spectroscopy.

X-PEEM microanalysis of inclusions in minerals

Inclusions in minerals are indicative of the environment and conditions of mineral formation and subsequent history. In some circumstances, evidence of earlier history is also present. We have studied several detrital zircon crystals from metaconglomerate in the Jack Hills, Western Australia (Peck et al. 2001) with the aim of identifying silicate inclusions. Many inclusions in these zircons measure 1 μm or less in diameter, and no other non-destructive analytical technique matches X-PEEM for spatial resolution. Figure 7 shows one such analysis on a 100 μm zircon, in which a pure quartz inclusion, approximately 7 μm × 3.5 μm in size, is identified and mapped with submicrometer resolution, at the Si$L_{2,3}$ edge. We demonstrate that inclusions substantially smaller than this can be analyzed by presenting the XANES from a single image pixel within the inclusion, corresponding to a 35 nm × 35 nm area on the specimen surface (~15 Å probing depth at the Si$L_{2,3}$ edge). This inclusion is easily identified as quartz by comparison with our reference spectrum. There is also a good match between the X-PEEM and the reference zircon spectra, but there are discrepancies in the relative intensities of the three main peaks. In fact, the X-PEEM spectrum from zircon (Fig. 7) is closer than our reference spectra (Figs. 2 and 7) to an earlier published zircon spectrum obtained with EELS (Garvie and Buseck 1999). When tested on a single sample, XANES spectra acquired in X-PEEM are identical to those acquired with the TEY method, and so further analysis will be required to determine the significance of these differences.

It is possible to map the distribution of the different silicate species. In Figure 7, the zircon distribution map was obtained by digital ratio of a 16 bit image acquired with SPHINX at 111 eV (on top of a zircon peak) by the pre-peak image at 109.8 eV. The ratio distribution map is displayed in blue, and digitally fused with the quartz map (in pink, ratio of images at 106.2 eV and 104.8 eV). Digital image ratioing is a simple procedure to map regions that correspond to different spectral lineshapes. Several alternative, and more quantitative, methods exist (Buckley et al. 1997; Koprinarov et al. 2002; Frazer et al. 2003) but combining images at photon energies chosen with reference to the XANES spectra allows quartz and zircon to be distinguished visually.

There is a region that partially surrounds the quartz inclusion from which no Si$L_{2,3}$ signal was obtained in X-PEEM. A map of the no-Si region is shown in brown, obtained from the ratio of images at 127 eV and 104 eV. The white areas were inaccessible to X-PEEM analysis due to topographic effects and the shadowing of the X-ray beam at the edges. We performed an additional SEM study of this region with energy dispersive X-ray (EDX) analysis. The region was confirmed to be a pit around most of the quartz inclusion, and contained a considerable amount of carbon, presumably coating the bottom of the pit. SEM-EDX has a probing depth greater than 1 μm, and could analyze the material beneath. By contrast, the X-PEEM technique is highly surface sensitive and cannot penetrate to the mineral beneath the surface contamination. SEM-EDX analysis indicates that the mineral in the pit is an Al-containing silicate mineral.

SUMMARY REMARKS

This quartz inclusion in zircon is an example of our new mineral mapping analysis, and it can be extended to a large

number of different mineral inclusions, provided they have characteristic spectral features that distinguish them from the surrounding mineral. Two minerals with indistinguishable spectra, e.g., albite and andesine at the Si$L_{2,3}$ edge, could not be mapped with this approach. On the other hand, mapping $L_{2,3}$ edges of Al (at 76 eV) and Ca (at 350 eV), or the *K* edge of Na (at 1071 eV) may be successful in distinguishing these two minerals at the sub-micrometer level. A synchrotron beamline with a wide energy range is therefore instrumental for spectromicroscopy analysis, such as the HERMON beamline at the UW-SRC, which encompasses the range 62–1300 eV.

By comparing X-ray absorption spectra fine-structure at the Si and O edges of common silicate minerals, we can discriminate among the samples studied. Despite some limitations, the ability to detect an individual or a group of silicates with confidence is expected to be valuable for analyses of submicrometer particles or inclusions in geological samples. This analysis can be used for mineral identification and imaging, provided that the minerals differ sufficiently in elemental composition, elemental oxidation state, or crystal structure.

Further work is required to understand the XANES of silicates. Large data sets and theoretical calculations are indispensable in making the correct connection between XANES and crystal structure. Real-space multiple-scattering theory is the approach of choice, as electronic structure output can be compared with alternative calculations, and the link to structural parameters is immediate.

ACKNOWLEDGMENTS

We are indebted to Simon Wilde for providing the zircon sample of Fig. 7. This work is based upon research conducted at the Synchrotron Radiation Center, University of Wisconsin-Madison, which is supported by the NSF under Award no. DMR- 0084402. We are indebted to the UW-Madison Department of Physics and Graduate School for supporting these experiments. We thank Astrid Jurgensen for assistance with the DCM beamline.

REFERENCES CITED

Bauer, E. (2001) Photoelectron Microscopy. Journal of Physics-Condensed Matter, 13, 11391–11404.

Buckley, C.J., Khaleque, N., Bellamy, S.J., Robins, M., and Zhang, X. (1997) Mapping the organic and inorganic components of tissue using NEXAFS. Journal de Physique IV 7 (C2 Part 1), 83.

Calas, G., Brown, G.E. Jr., Waychunas, G.A., and Petiau, J. (1987) X-ray absorption spectroscopic studies of silicate glasses and minerals. Physics and Chemistry of Minerals, 15, 19–29.

de Jong, B.H.W.S. and Brown, G.E. Jr. (1980) Polymerization of silicate and aluminate tetrahedra in glasses, melts and aqueous solutions—I. Electronic structure of H_6SiO_7, $H_6AlSiO_7^-$, and $H_6Al_2O_7^{2-}$. Geochimica et Cosmochimica Acta, 44, 491–511.

De Stasio, G., Capozi, M., Lorusso, G.F., Baudat, P.A., Droubay, T.C., Perfetti, P., Margaritondo, G., and Tonner, B.P. (1998) MEPHISTO: Performance tests of a novel synchrotron imaging photoelectron spectromicroscope. Review of Scientific Instruments, 69, 2062–2067.

De Stasio, G., Gilbert, B., Frazer, B.H., Nealson, K.H., Conrad, P.G., Livi, V., Labrenz, M., and Banfield, J.F. (2001) The multidisciplinarity of spectromicroscopy: from geomicrobiology to archaeology. Journal of Electron Spectroscopy and Related Phenomena, 114, 997–1003.

Frazer, B.H., Sonderegger, B.R., Gilbert, B., Richter, K.L., Salt, C., Wiese, L., Rajeshf, D., Howard, S.P., Fowler, J.F., Mehta, M.P., and De Stasio, G. (2003) Mapping of Physiological and Trace elements with X-PEEM, Proceedings of the 2002 X-Ray Microscopy Conference, Journal de Physique IV, in press.

Garvie, L.A.J. and Buseck, P.R. (1999) Bonding in silicates: Investigation of the Si $L_{2,3}$ edge by parallel electron energy-loss spectroscopy. American Mineralogist, 84, 946–964.

Garvie, L.A.J., Rez, P., Alvarez, J.R., Buseck, P.R., Craven, A.J., and Brydson, R. (2000) Bonding in alpha-quartz (SiO_2): A view of the unoccupied states. American Mineralogist, 85, 732–738.

Geisinger, K.L., Gibbs, G.V., and Navrotsky, A. (1985) A molecular orbital study of bond length and angular variations in framework structures. Physics and Chemistry of Minerals, 11, 266–283.

Gibbs, G.V. (1982) Molecules as models for bonding in silicates. American Mineralogist, 67, 421–450.

Gilbert, B., Frazer, B.H., Zhang, H., Huang, F., Banfield, J.F., Haskel, D., Lang, J.C., Srajer, G., and De Stasio, G. (2002) X-ray absorption spectroscopy of the cubic and hexagonal polytypes of zinc sulfide. Physical Review B, 66, 245205.

Grush, M.M., Chen, J., Stemmler, T.L., George, S.J., Ralston, C.Y., Stilbrany, R.T., Gelasco, A., Christou, G., Gorun, S.M., Penner-Hahn, J.E., Cramer, S.P. Journal of the American Chemical Society, 118, 65.

Hoffman, A., Folman, M., and Prawler, S. (1991) Secondary-electron-emission spectrum of diamond. Physical Review B, 44, 4640–4643.

Kisiel, A., Dalba, G., Fornasini, P., Podgorny, M., Oleszkiewicz, J., Rocca, F., and Burattini, E. (1989) X-ray absorption spectroscopy of ZnTe, CdTe, and HgTe: Experimental and theoretical study of near-edge structures. Physical Review B, 39, 7895–7904.

Koprinarov, I.N., Hitchcock, A.P., McCrory, C., and Childs, R.F. (2002) Quantitative mapping of structured polymeric systems using singular value decomposition analysis of soft X-ray images. Journal of Physical Chemistry B, 106, 5358–5364.

Li, D., Bancroft, G.M., Kasrai, M., Fleet, M.E., Secco, R.A., Feng, X.H., Tan, K.H., and Yang, B.X. (1994) X-ray absorption of silicon dioxide (SiO_2) polymorphs: the structural characterization of opal. American Mineralogist, 79, 622–632.

Li, D., Bancroft, G.M., Fleet, M.E., and Feng, X.H. (1995) Silicon K-edge XANES spectra of silicate minerals. Physics and Chemistry of Minerals, 22, 115–122.

Li, Y.P. and Ching, W.Y. (1985) Band structures of all polycrystalline forms of silicon dioxide. Physical Review B, 31, 2172–2179.

McComb, D.W., Hansen, P.L., and Brydson, R. (1991) A study of silicon ELNES in nesosilicates. Microscopy, Microanalysis, Microstructures, 2, 561–568.

McComb, D.W., Brydson, R., Hansen, P.L., and Payne, R.S. (1992) Qualitative interpretation of electron energy-loss near-edge structure in natural zircon. Journal of Physics-Condensed Matter, 4, 8363–8374.

Peck, W.H., Valley, J.W., Wilde, S.A., and Graham, C.M. (2001) Oxygen isotope ratios and rare earth elements in 3.3 to 4.4 Ga zircons: ion microprobe evidence for high $\delta^{18}O$ continental crust in the early Archean. Geochimica et Cosmochimica Acta, 65, 4215–4229.

Rehr, J.J. and Albers, R.C. (2000) Theoretical approaches to X-ray absorption fine structure. Reviews of Modern Physics, 72, 621–653.

Soldatov, A.V., Kasrai, M., and Bancroft, G.M. (2000) Unoccupied electronic states of stishovite: X-ray absorption fine structure theoretical analysis. Solid State Communications, 115, 687–692.

Sutherland, D.G.J., Kasrai, M. Bancroft, G.M., Lui, Z.F., and Tan, K.H. (1993) Si L- and K- edge absorption near edge spectroscopy of gas-phase $Si(CH_3)_x(OCH_3)_{4-x}$: models for solid state analogs. Physical Review B, 48, 14989–15001.

Tanaka, I., Kawai, J., and Adachi, H., (1995) Near-edge X-ray absorption fine structure of crystalline silicon dioxides. Physical Review B, 52, 11733–11739.

Tossell, J.A. (1975) The electronic structures of silicon, aluminum, and magnesium in tetrahedral coordination with oxygen from SCF-Xα-MO calculation. Journal of the American Chemical Society, 97, 4840–4844.

Wang, H., Peng, G., Miller, L.M., Scheuring, E.M., George, S.J., Chance, M.R., and Cramer, S.P. (1997) Iron L-edge X-ray absorption spectroscopy of myoglobin complexes and photolysis products. Journal of the American Chemical Society, 119, 4921–4928.

Westre, T.E., Kennepohl, P., DeWitt, J.G., Hedman, B., Hodgson, K.O., and Solomon, E.I. (1997) A multiplet analysis of Fe K edge 1s-3d pre-edge features of iron complexes. Journal of the American Chemical Society, 119, 6297–6314.

Wiech, G. and Kurmaev, E.Z. (1985) X-ray emission bands and electronic structure of crystalline and vitreous silica. Journal of Physics C: Solid State Physics, 18, 4393–4402.

Wilke, M., Farges, F., Petit, P.E., Brown, G.E., and Martin, F. (2001) Oxidation state and coordination of Fe in minerals: An FeK-XANES spectroscopic study. American Mineralogist, 86, 714–730.

Wu, Z.Y., Jollet, F., and Seifert, F. (1998) Electronic structure analysis of α-SiO_2 via X-ray absorption near-edge structure at the Si K, $L_{2,3}$ and O K edges. Journal of Physics-Condensed Matter, 10, 8083–8092.

MANUSCRIPT RECEIVED JUNE 10, 2002
MANUSCRIPT ACCEPTED JANUARY 8, 2003
MANUSCRIPT HANDLED BY ROBERT DYMEK